catalysts

MDPI

Article

Efficient Electron Transfer in g-C_3N_4/TiO_2 Heterojunction for Enhanced Photocatalytic CO_2 Reduction

Peng Jiang [1,*], Yang Yu [2,*], Kun Wang [1] and Wenrui Liu [1]

[1] State Key Laboratory of Advanced Technology for Materials Synthesis and Processing, Wuhan University of Technology, Wuhan 430070, China; kkkun@whut.edu.cn (K.W.); liuwenrui@whut.edu.cn (W.L.)
[2] Centre for Infrastructure Engineering and Safety, School of Civil and Environmental Engineering, The University of New South Wales, Sydney, NSW 2052, Australia
* Correspondence: pengjiang@whut.edu.cn (P.J.); yang.yu@uts.edu.au (Y.Y.)

Abstract: Excessive emissions of carbon dioxide have led to the greenhouse effect and global warming. Reducing carbon dioxide into high-value-added chemicals through solar energy is a promising approach. Herein, a g-C_3N_4/TiO_2 heterojunction photocatalyst with efficient electron transfer is designed for photocatalytic CO_2 reduction. The CH_4 (18.32 $\mu mol \cdot h^{-1} \cdot g^{-1}$) and CO (25.35 $\mu mol \cdot h^{-1} \cdot g^{-1}$) evolution rates of g-$C_3N_4$/$TiO_2$ are higher than those of g-C_3N_4 and TiO_2. The enhanced photocatalytic CO_2 reduction performance is attributed to the efficient charge carrier transfer in the g-C_3N_4/TiO_2 heterojunction. The electron transfer route was verified by in situ irradiated X-ray photoelectron spectroscopy (XPS). The photocatalytic CO_2 reduction mechanism on g-C_3N_4/TiO_2 was investigated by in situ diffuse reflectance infrared Fourier transform spectroscopy (DRIFTS). This work provides a strategy for designing a polymer/metallic oxide heterojunction with efficient electron transfer for enhanced photocatalytic CO_2 reduction.

Keywords: g-C_3N_4/TiO_2; heterojunction; photocatalytic CO_2 reduction; polymer/metallic oxide

check for updates

Citation: Jiang, P.; Yu, Y.; Wang, K.; Liu, W. Efficient Electron Transfer in g-C_3N_4/TiO_2 Heterojunction for Enhanced Photocatalytic CO_2 Reduction. *Catalysts* **2024**, *14*, 335. https://doi.org/10.3390/catal14060335

Academic Editor: Akira Nishimura

Received: 22 April 2024
Revised: 15 May 2024
Accepted: 20 May 2024
Published: 22 May 2024

1. Introduction

With the rapid development of society and economy, the mass consumption of fossil fuels has caused severe environmental pollution and led to sharp declines in their reserves. The excessive emissions of carbon dioxide (CO_2) in recent years have resulted in serious environmental issues, such as the greenhouse effect, global warming, sea ice melting, and sea-level rise [1–4]. It is urgent to eliminate CO_2 in the atmosphere for sustainable development. The conversion of CO_2 into high-value-added chemicals and fuels eliminates CO_2 in the atmosphere, solves the energy crisis, and reduces environmental pollution. Converting CO_2 into high-value-added chemicals by solar energy is a promising approach which is environmentally benign [5–8]. Solar energy being an abundant renewable resource is the powerful motivation to employ photocatalytic CO_2 reduction to produce high-value-added chemicals and fuels.

The CO_2 molecule is chemically stable and inert under normal conditions. Therefore, the activation of CO_2 by solar energy usually requires a photocatalyst to overcome the thermodynamic energy barrier. Metal dioxide semiconductors, polymer semiconductors, and organic semiconductors are widely used as photocatalysts for photocatalytic CO_2 reduction. However, it is necessary to address issues such as the rapid recombination of photogenerated electron–hole pairs, as well as the poor photoredox ability of charge carriers, to improve the photocatalytic performance of semiconductor photocatalysts. Designing semiconductor/semiconductor interfaces for heterojunction materials can improve the efficiency of spatial charge separation, thereby suppressing charge carrier recombination and enhancing photocatalytic performance [9–12]. A heterojunction is an interface region formed by the contact of two different semiconductors. According to the conductive types of the two materials, heterojunctions can be divided into homojunctions (P-p junctions or N-n junctions) and heterojunctions (P-n or p-N junctions). Multilayer heterojunctions are called heterostructures. Therefore, heterojunction materials have become a promising solution to address the limitations of traditional photocatalysis.

Single photocatalysts suffer from unsatisfactory photocatalytic activity due to the rapid recombination of the photogenerated electrons and holes. As is well known, constructing heterojunctions can realize improved photocatalytic activity due to the enhanced separation and transfer of the photogenerated electrons and holes. Specifically, the construction of heterojunctions is a promising strategy to enhance photocatalytic CO_2 reduction performance. Generally, a heterojunction consists of a reduction photocatalyst (RP) and an oxidation photocatalyst (OP). Driven by band bending and internal electric field (IEF), the electrons transfer between the RP and OP, leading to the photogenerated electrons of the RP with strong reduction ability and the photogenerated holes of the OP with strong oxidation. Therefore, the heterojunction structure can promote charge carrier transfer and improve photocatalytic CO_2 reduction performance.

Polymer semiconductor materials are organic electronic materials composed of polymer compounds that have semiconductor properties and can be used to make semiconductor devices and integrated circuits. As a promising polymer semiconductor, graphitic carbon nitride (g-C_3N_4) has attracted increasing attention in photocatalysis due to its low cost, high thermal and chemical stability, easy preparation process, semiconductivity, and appropriate band gap [13–16]. Among various semiconductor photocatalysts, titanium dioxide (TiO_2) has been widely used as a photocatalyst due to its non-toxicity, low cost, excellent sunlight harvesting capability, and high chemical stability [17–20]. Thus, g-C_3N_4 and TiO_2 are widely used as catalysts for photocatalytic CO_2 reduction to produce high-value-added chemicals by solar energy. However, g-C_3N_4 and TiO_2 suffer from low photocatalytic activity owing to their poor photoreduction ability and fast recombination of photogenerated electrons and holes. Constructing a g-C_3N_4/TiO_2 heterojunction for enhancing photocatalytic CO_2 reduction is a feasible and effective approach [21–35]. Due to the different energy band potentials, the coupling of g-C_3N_4 and TiO_2 is expected to form a g-C_3N_4/TiO_2 heterojunction which can promote the separation and transfer of the photogenerated electrons and holes, thereby improving the photocatalytic CO_2 reduction activity.

Herein, the g-C_3N_4/TiO_2 heterojunction is designed for enhanced photocatalytic CO_2 reduction. The g-C_3N_4/TiO_2 heterojunction photocatalyst exhibits higher CH_4 (18.32 μmol·h^{-1}·g^{-1}) and CO (25.35 μmol·h^{-1}·g^{-1}) evolution rates, compared with g-C_3N_4 and TiO_2. Although the g-C_3N_4/TiO_2 heterojunction has promising prospects for enhanced photocatalytic CO_2 reduction activity, the underlying mechanisms of the charge transfer and CO_2 reduction pathways remain unknown. In this regard, we applied in situ irradiated X-ray photoelectron spectroscopy (XPS) to investigate the electron transfer in the g-C_3N_4/TiO_2 heterojunction and in suit diffuse reflectance infrared Fourier transform spectroscopy (DRIFTS) to detect the pathway of CO_2 reduction on the surface of the g-C_3N_4/TiO_2 photocatalyst during photocatalytic CO_2 reduction. The efficient electron transfer in the g-C_3N_4/TiO_2 heterojunction improved the photocatalytic CO_2 reduction performance, which provides a promising approach to designing polymers/metal dioxide photocatalysts with efficient electron transfer for enhanced photocatalytic CO_2 reduction.

2. Results and Discussion

2.1. Microstructure and Analysis of Physical Properties

TiO_2 was dispersed on g-C_3N_4 to form a g-C_3N_4/TiO_2 heterojunction (Figure 1a). Field-emission scanning electron microscopy (FSEM) was applied to investigate the microstructure of the photocatalysts. The microstructures of g-C_3N_4 and TiO_2 are shown in Figures S1 and S2. g-C_3N_4 shows a big bulk structure with a size of 5–10 μm, while TiO_2 is a small bulk structure with a size of 0.5–1 μm. As Figure 1b,c show, TiO_2 is uniformly dispersed on the surface of g-C_3N_4, which implies the successful loading of TiO_2 onto g-C_3N_4. The high-resolution TEM (HRTEM) image suggests that the lattice–fringe spacing of 0.35 nm is indexed into the (101) plane of TiO_2 (Figure 1d), indicating the existence of

TiO_2 in the g-C_3N_4/TiO_2 heterojunction. The X-ray powder diffraction (XRD) patterns were employed to study the phase structures of the samples. As shown in Figure 1e, the XRD patterns correspond to typical anatase TiO_2 and g-C_3N_4. The peaks of g-C_3N_4 and TiO_2 can be observed in g-C_3N_4/TiO_2, which implies that TiO_2 was successfully loaded onto g-C_3N_4 [13,20]. According to the XRD patterns, the average crystallite size of TiO_2 was 55 nm. The above results indicate the g-C_3N_4/TiO_2 heterojunction photocatalyst was successfully prepared. The nitrogen adsorption–desorption isotherms of g-C_3N_4, TiO_2, and g-C_3N_4/TiO_2 display typical type IV isotherms with the type H_3 hysteresis loop (Figure 1f). The pore size distribution curves of g-C_3N_4, TiO_2, and g-C_3N_4/TiO_2 indicate that the photocatalysts have abundant mesoporous structures (Figure S1). The Brunauer–Emmett–Teller surface areas (S_{BET}) of g-C_3N_4, TiO_2, and g-C_3N_4/TiO_2 were 8.2, 11.2, and 10.1 $m^2 \cdot g^{-1}$, respectively (Table S1).

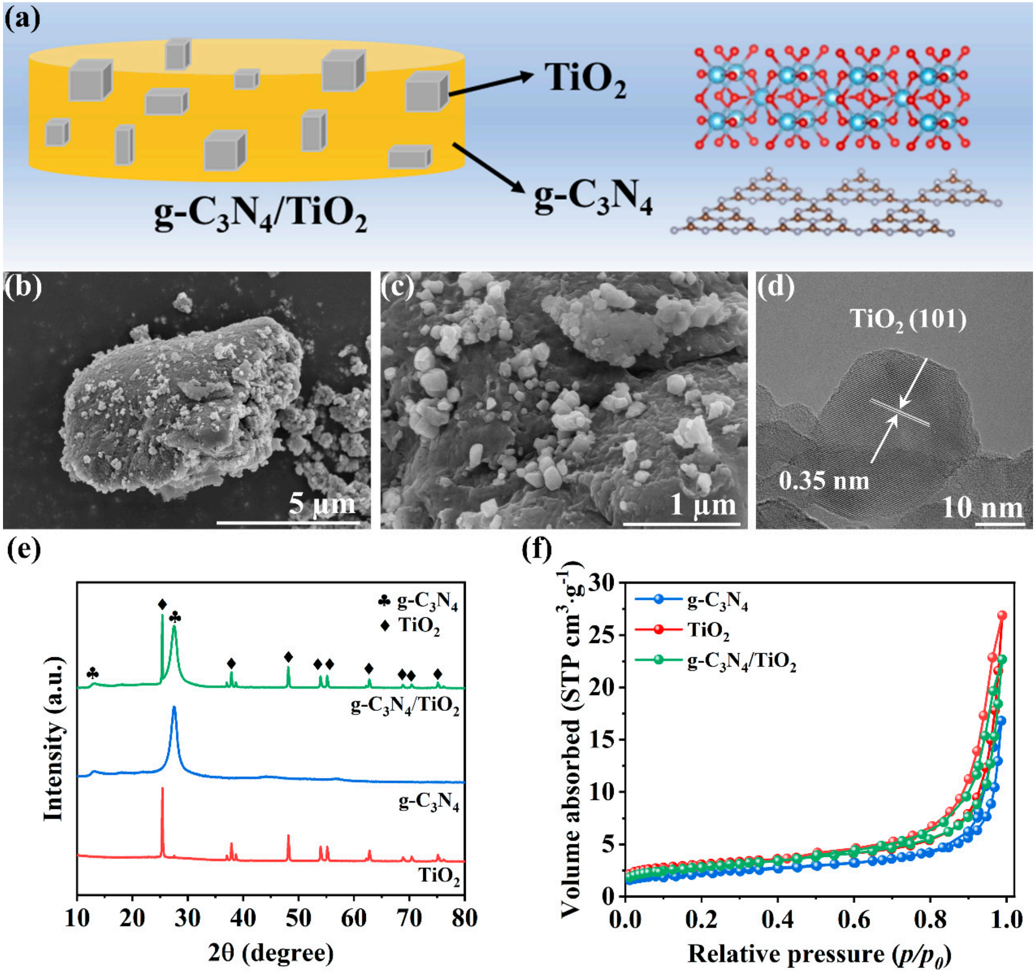

Figure 1. (**a**) Scheme of g-C_3N_4/TiO_2; (**b**,**c**) FSEM images of g-C_3N_4/TiO_2; (**d**) high-resolution TEM (HRTEM) image of g-C_3N_4/TiO_2; (**e**) XRD patterns of g-C_3N_4, TiO_2, and g-C_3N_4/TiO_2; (**f**) nitrogen adsorption–desorption isotherms of g-C_3N_4, TiO_2, and g-C_3N_4/TiO_2.

To determine the light absorption of g-C_3N_4, TiO_2, and g-C_3N_4/TiO_2, the UV–vis diffuse reflectance spectra (UV–vis DRS) were measured. From Figure 2a, compared with TiO_2, the absorption edge of g-C_3N_4/TiO_2 shows a red shift. The absorption of g-C_3N_4 in the 350–520 nm region is stronger, which leads to g-C_3N_4/TiO_2 enhancing the response to visible light. Meanwhile, compared with g-C_3N_4, the absorption of TiO_2 in the ultraviolet region is stronger than that of g-C_3N_4; thus, g-C_3N_4/TiO_2 improves absorption in the ultraviolet region. The result of the UV–vis DRS indicates strong ultraviolet–visible light absorption ability for g-C_3N_4/TiO_2, which is advantageous for photocatalytic CO_2

reduction. According to the Tauc plots (Figure 2b), the band gaps (Eg) of g-C_3N_4 and TiO_2 were 2.55 and 3.05 eV, respectively. From the Mott–Schottky (M-S) curves, the flat-band potentials (E_{fb}) of g-C_3N_4 and TiO_2 were −0.97 and −0.55 eV (V vs. Ag/AgCl), respectively (Figure 2c). With reference to normal hydrogen electrode (NHE), the flat-band potentials (E_{fb}) of g-C_3N_4 and TiO_2 were −0.77 and −0.35 eV, respectively [36–39]. Generally, for n-type semiconductors, the E_{fb} roughly equals to the conduction band (CB) potential. Therefore, according to the formula $E_g = E_{vb} - E_{cb}$, the valence band (VB) potentials of g-C_3N_4 and TiO_2 were 1.78 and 2.70 eV, respectively [40–43]. The estimated band structures of g-C_3N_4 and TiO_2 are shown in Figure 2d.

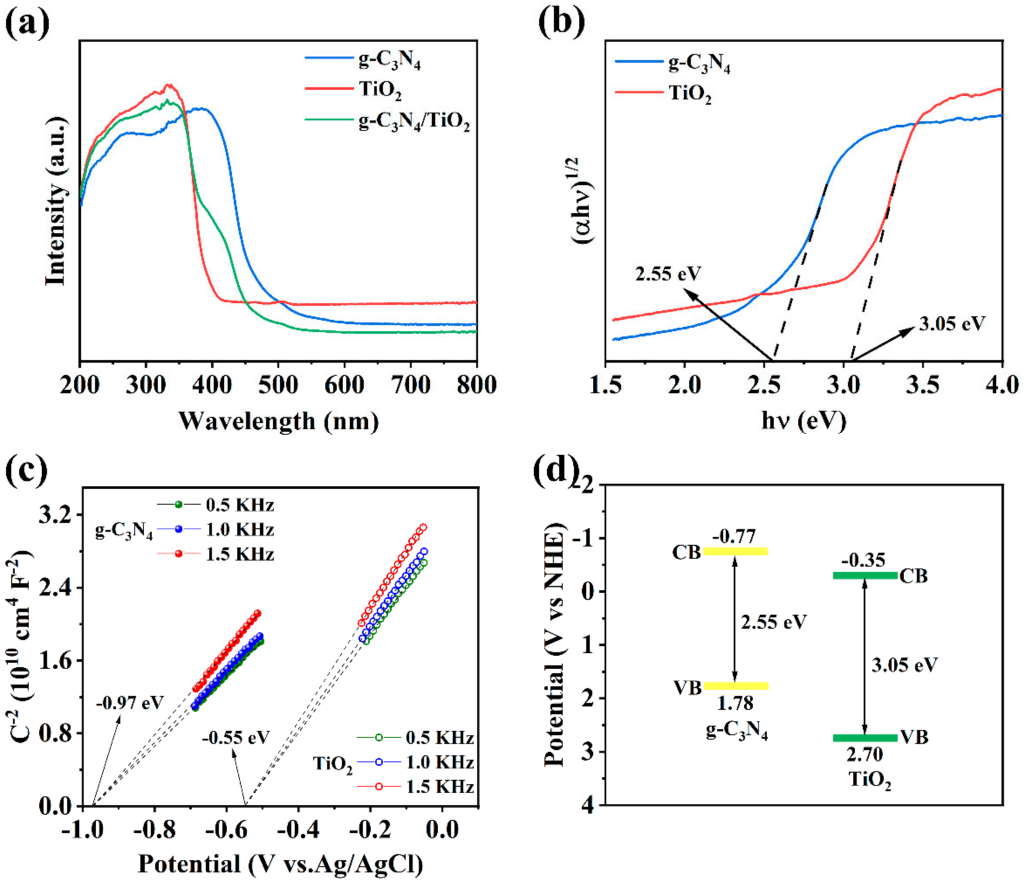

Figure 2. (**a**) UV–vis DRS of g-C_3N_4, TiO_2, and g-C_3N_4/TiO_2; (**b**) Tauc plots of g-C_3N_4, TiO_2, and g-C_3N_4/TiO_2; (**c**) M-S plots of g-C_3N_4, and TiO_2; (**d**) estimated band structures of g-C_3N_4 and TiO_2.

2.2. Electron Transfer Route

X-ray photoelectron spectroscopy (XPS) was employed to identify the surface elements and electronic chemical states of the photocatalysts. As presented in Figure S3, XPS survey spectra show that C, N, Ti, and O elements can be detected in g-C_3N_4/TiO_2, indicating that the g-C_3N_4/TiO_2 heterojunction was successfully prepared. In Figure 3a, the peaks centered at 458.7 and 464.4 eV can be assigned to the $2p_{3/2}$ and $2p_{1/2}$ states of Ti^{4+} in TiO_2, respectively. Additionally, the peaks located at 530.8 and 531.9 eV are attributed to the Ti-O bond and −OH group, respectively (Figure 3b). For g-C_3N_4, the peaks centered at 399.3, 400.0, and 401.7 eV can be ascribed to C-N=C, N-$(C)_3$, and C-N-H, respectively. In general, the change in electron binding energy reflects the change in electron density. Therefore, the change in electron binding energy can verify the direction of charge carrier transfer in heterojunction photocatalysts [44–46]. As shown in Figure 3a,b, the binding energies of Ti 2p and O 1s in g-C_3N_4/TiO_2 shift toward higher energy levels, indicating loss of electrons for TiO_2. Compared with g-C_3N_4, the binding energy of N 1s in g-C_3N_4/TiO_2 shifts to a lower energy level, implying that g-C_3N_4 gains electrons (Figure 3c). The electrons migrate from TiO_2 to g-C_3N_4 in the g-C_3N_4/TiO_2 heterojunction. The binding energies of Ti 2p and O 1s in g-C_3N_4/TiO_2 shift toward lower energy levels under light irradiation, while the binding energy of N 1s shift to a higher energy level. The in situ high-resolution XPS data indicate the photogenerated electron transfer from g-C_3N_4 to TiO_2.

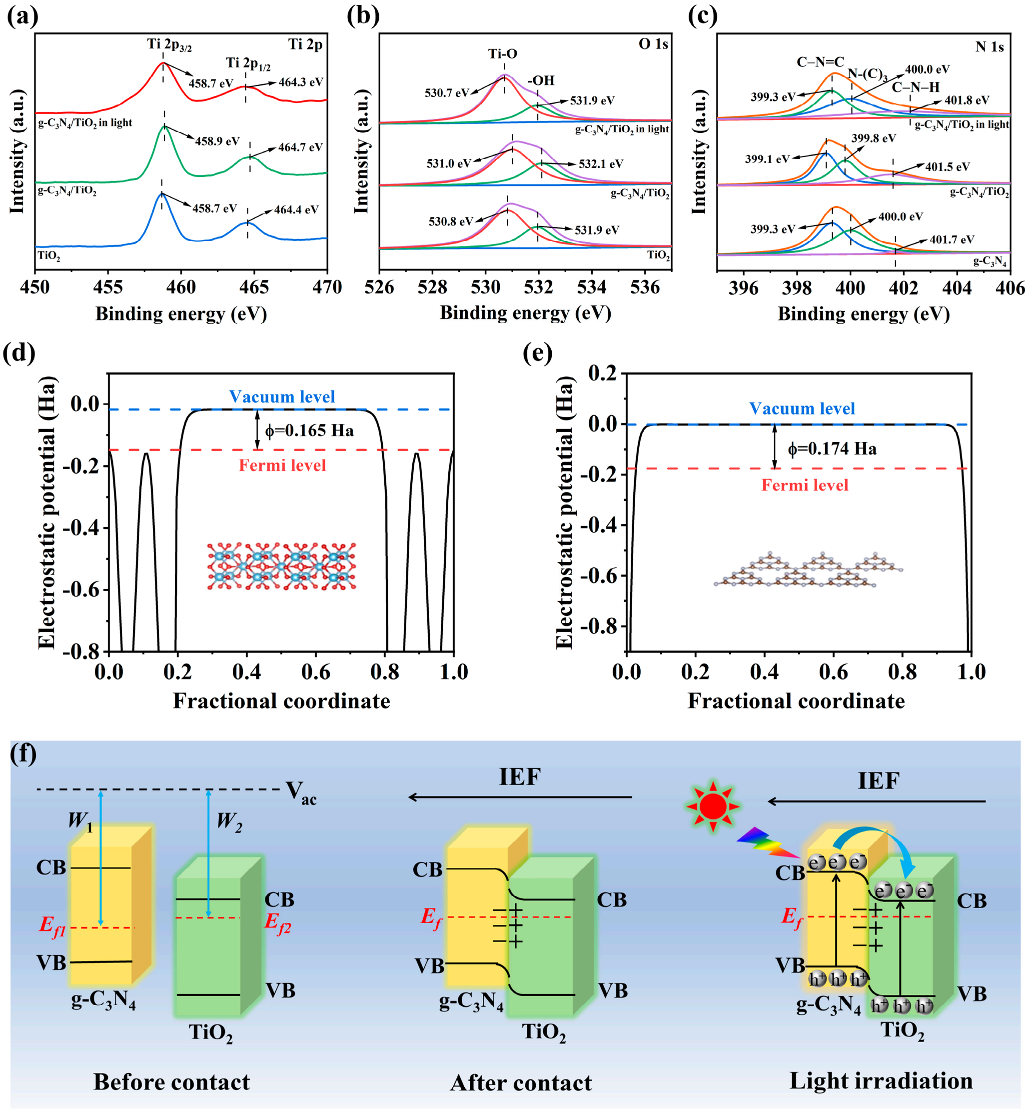

Figure 3. In situ high-resolution XPS results of (**a**) Ti 2p, (**b**) O 1s, and (**c**) N 1s of g-C_3N_4, TiO_2, and g-C_3N_4/TiO_2; work functions of (**d**) TiO_2 and (**e**) g-C_3N_4; (**f**) schematic illustrations of electron transfer mechanism between g-C_3N_4 and TiO_2 before contact, after contact, and after contact under light irradiation.

On account of the results of in situ irradiated XPS, the electron transfer route between g-C_3N_4 and TiO_2 is proposed. The work functions (Φ) of g-C_3N_4 and TiO_2 were calculated by density functional theory (DFT). Figure 3d,e show that the work function of g-C_3N_4 (0.174 Ha) is larger than that of TiO_2 (0.165 Ha), which indicates that the Fermi level of TiO_2 is higher than that of g-C_3N_4. As shown in Figure 3f, before the formation of the g-C_3N_4/TiO_2 heterojunction, g-C_3N_4 has larger W_1 and lower E_{f1}, while TiO_2 has smaller W_2 and higher E_{f2}. The difference in work function will lead to band bending and internal electric field (IEF) at the interface between g-C_3N_4 and TiO_2. After the contact of g-C_3N_4 with TiO_2, the g-C_3N_4/TiO_2 heterojunction forms, with the electron transfer from TiO_2 to g-C_3N_4 being driven by the IEF. When the g-C_3N_4/TiO_2 heterojunction is under light irradiation, the electrons are excited from the VB to the CB of g-C_3N_4 and TiO_2, respectively.

Then, the photogenerated electrons migrate from the CB of g-C_3N_4 to the CB of TiO_2 and the holes transfer from the VB of TiO_2 to the VB of g-C_3N_4, leading to the efficient separation and transfer of the photogenerated electron–hole pairs. The efficient separation and transfer of the photogenerated electron–hole pairs in the heterojunction is crucial to the improvement in photocatalytic CO_2 reduction performance. The photogenerated electrons of the RP with strong reduction ability in TiO_2 and the photogenerated holes of the OP with strong oxidation ability in g-C_3N_4 are preserved.

Photocurrent in semiconductors is caused by light irradiation. When materials are under light irradiation, the photon excites the electrons in the valence band of the semiconductor to the conduction band and generates an electric current. Electrochemical impedance is the electrical resistance during charge carrier transport in photocatalysts. Transient photocurrent spectra (TPC) and electrochemical impedance spectroscopy (EIS) data can be used to examine charge carrier separation and transfer behavior in a photocatalyst. As can be seen in Figure 4a, the photocurrent density of g-C_3N_4/TiO_2 is larger than those of g-C_3N_4 and TiO_2. g-C_3N_4/TiO_2 shows a smaller electrochemical impedance spectroscopy radius than g-C_3N_4 and TiO_2 (Figure 4b). The results of TPC and EIS illustrate efficient photogenerated charge carrier separation and transfer in the g-C_3N_4/TiO_2 heterojunction. The fluorescence lifetimes of g-C_3N_4, TiO_2, and g-C_3N_4/TiO_2 are shown in Figure S5. The average lifetimes (τ_{ave}) of the photocarriers in g-C_3N_4, TiO_2, and g-C_3N_4/TiO_2 are 2.85, 1.85, and 1.15 ns, respectively. The results of fluorescence lifetime indicate enhanced electron separation and transfer process in the g-C_3N_4/TiO_2 heterojunction.

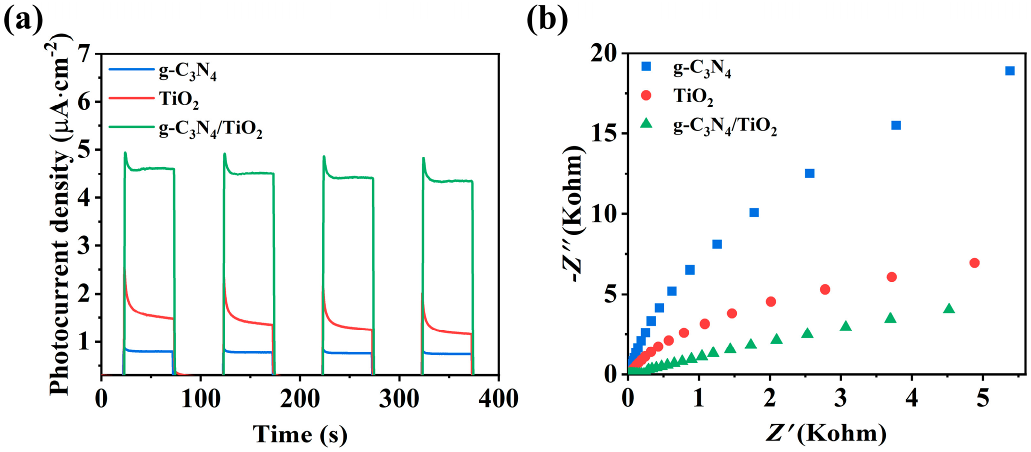

Figure 4. (**a**) Transient photocurrent spectra (TPC) and (**b**) electrochemical impedance spectroscopy (EIS) results of g-C_3N_4, TiO_2, and g-C_3N_4/TiO_2.

2.3. Photocatalytic CO_2 Reduction Performance

The photocatalytic CO_2 reduction performances of different photocatalysts were measured under UV–vis light. As presented in Figure 5a, CH_4 and CO are the major photoreduction products in the photocatalytic CO_2 reduction processes of g-C_3N_4, TiO_2, and g-C_3N_4/TiO_2. The CH_4 and CO evolution rates of g-C_3N_4/TiO_2 are up to 18.32 and 25.35 $\mu mol \cdot h^{-1} \cdot g^{-1}$, respectively, while the CH_4 evolution rates of g-C_3N_4 and TiO_2 are 7.32 and 2.07 $\mu mol \cdot h^{-1} \cdot g^{-1}$, respectively. The CH_4 evolution rates of g-C_3N_4/TiO_2 are 2.5 and 8.9 times larger than those of g-C_3N_4 and TiO_2, respectively. The CO evolution rates of g-C_3N_4 and TiO_2 are 1.63 and 16.34 $\mu mol \cdot h^{-1} \cdot g^{-1}$, respectively. The CO evolution rates of g-C_3N_4/TiO_2 are 15.6 and 1.6 times larger than those of g-C_3N_4 and TiO_2, respectively. The CH_4 and CO evolution rates of g-C_3N_4/TiO_2 grow nearly linearly over time (Figure 5b,c) and are much higher than those of g-C_3N_4 and TiO_2 during photocatalytic CO_2 reduction. Compared with g-C_3N_4 and TiO_2, g-C_3N_4/TiO_2 exhibits excellent photocatalytic CO_2 reduction activity. Moreover, the photocatalytic CO_2 reduction performance of g-C_3N_4/TiO_2 is higher than those of many other photocatalysts under similar conditions (Table S2, Supporting Information). The CH_4 and CO yields of g-C_3N_4/TiO_2 exhibited minor changes during the cycled stability test (Figure 5d), and the crystal structure of g-C_3N_4/TiO_2 remained stable after the cycled stability test (Figures S6 and S7), indicating that g-C_3N_4/TiO_2 remains stable during photocatalytic CO_2 reduction. The CH_4 and CO evolution rates of g-C_3N_4/TiO_2 indicate that the efficient electron transfer in the g-C_3N_4/TiO_2 heterojunction leads to strong oxidation and reduction abilities, thereby improving the photocatalytic CO_2 reduction activity.

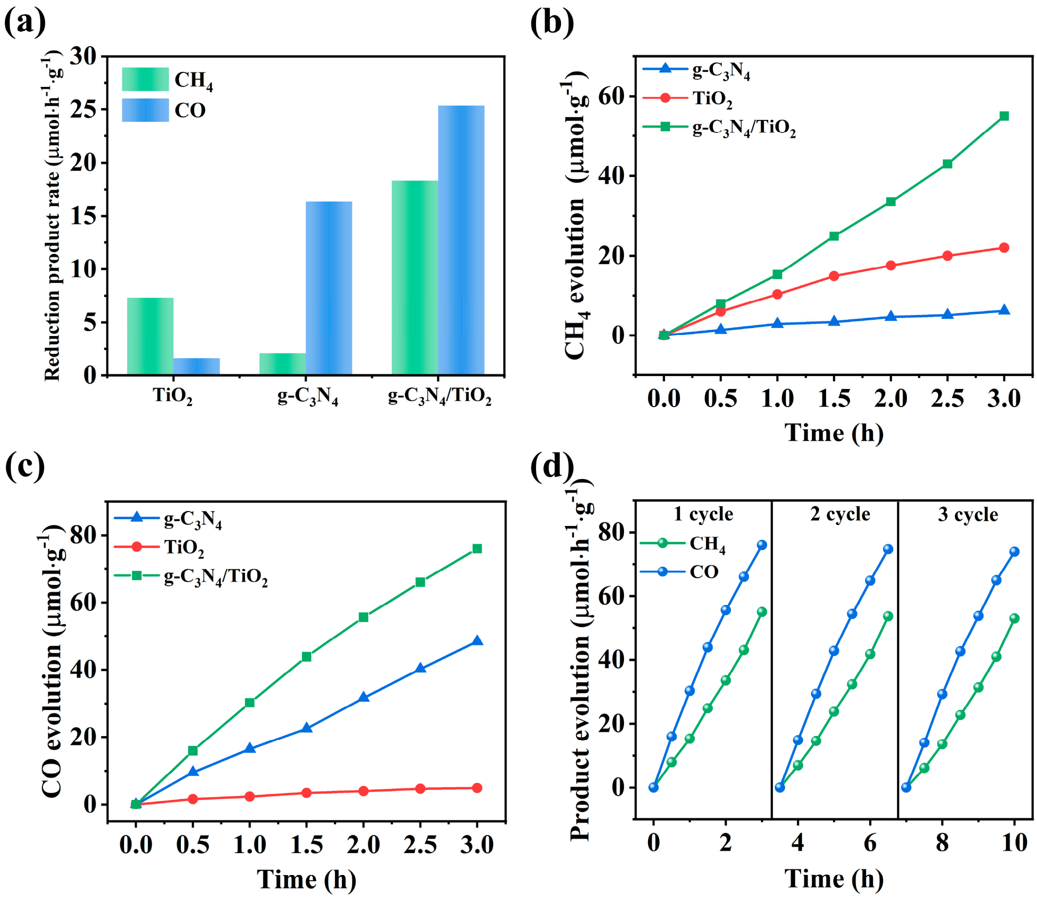

Figure 5. (**a**) Product evolution rate via photocatalytic CO_2 reduction reaction; (**b**) time-dependent CH_4 evolution; (**c**) time-dependent CO evolution of g-C_3N_4, TiO_2, and g-C_3N_4/TiO_2; (**d**) photocatalytic stability test of g-C_3N_4/TiO_2.

In situ diffuse reflectance infrared Fourier transform spectroscopy (DRIFTS) was performed to detect the CO_2 reduction pathway and possible reaction intermediates on the surface of the g-C_3N_4/TiO_2 photocatalyst during photocatalytic CO_2 reduction. The DRIFTS data of g-C_3N_4/TiO_2 in the dark and under light irradiation were collected during photocatalytic CO_2 reduction (Figure 6). Initially, no absorption peaks could be detected on the surface of the g-C_3N_4/TiO_2 photocatalyst in the dark (0 min). With the introduction of CO_2 and H_2 (10–30 min), monodentate carbonate species (m-CO_3^{2-}; 1303, 1424, 1489, and 1558 cm^{-1}) and bidentate carbonate species (b-CO_3^{2-}; 1520 and 1650 cm^{-1}) could be detected [40,43,47,48]. The existence of m-CO_3^{2-} and b-CO_3^{2-} indicates that CO_2 was successfully adsorbed and activated on the surface of g-C_3N_4/TiO_2. New peaks appeared in the spectroscopy under light irradiation (10–40 min). Carboxylate species (COO^-; 1339 and 1363 cm^{-1}), formaldehyde species ($HCHO^-$; 1507 and 1749 cm^{-1}), and methoxy groups (CH_3O^-; 1681, 1715 and 1731 cm^{-1}) were detected on the surface of the g-C_3N_4/TiO_2 photocatalyst during photocatalytic CO_2 reduction [43,47,49]. COO^-, $HCHO^-$, and CH_3O^- are the crucial reaction intermediates in the formation of CH_4 and CO. Thus, the proposed pathway for photocatalytic CO_2 reduction over g-C_3N_4/TiO_2 can be briefly expressed as follows: $CO_2 \rightarrow COO^- \rightarrow HCHO^- \rightarrow CH_3O^- \rightarrow CH_4$ and $CO_2 \rightarrow COO^- \rightarrow CO$. The $g\text{-}C_3N_4/TiO_2$ photocatalyst-induced process of the photocatalytic reduction of CO_2 to CH_4 and CO involves electron transfer steps that can be expressed as follows: $CO_2 + 8H^+ + 8e^- \rightarrow CH_4 + 2H_2O$ and $CO_2 + 2H^+ + 2e^- \rightarrow CO + H_2O$.

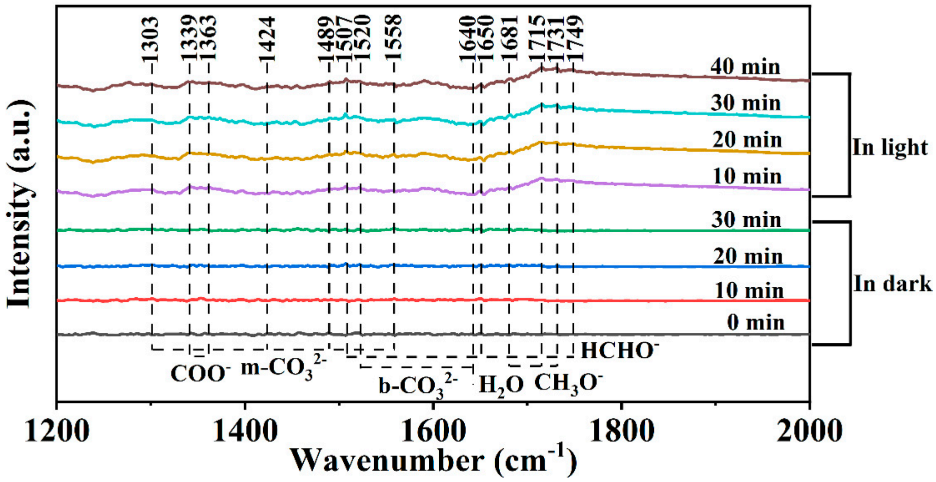

Figure 6. In situ diffuse reflectance infrared Fourier transform spectroscopy (DRIFTS) results of $g\text{-}C_3N_4/TiO_2$.

The mechanism of the N_4/TiO_2 heterojunction for photocatalytic CO_2 reduction can be summarized as follows (Figure 7): Firstly, when TiO_2 comes into contact with $g\text{-}C_3N_4$, electrons transfer from TiO_2 to $g\text{-}C_3N_4$ because of the different work function and Fermi level. Subsequently, $g\text{-}C_3N_4/TiO_2$ is exposed to light irradiation, and the photogenerated electrons are excited from the VB to the CB of $g\text{-}C_3N_4$ and TiO_2, respectively. Then, the photogenerated electrons of the CB of $g\text{-}C_3N_4$ migrate to the CB of TiO_2; the holes transfer from the VB of TiO_2 to the VB of $g\text{-}C_3N_4$, improving the separation and transfer of the photogenerated electron–hole pairs. The efficient electron transfer in the $g\text{-}C_3N_4/TiO_2$ heterojunction results in the photogenerated electrons of the RP with strong reduction ability in TiO_2 and the photogenerated holes of the OP with strong oxidation ability in $g\text{-}C_3N_4$. Meanwhile, H_2 is oxidized to H^+ on the VB of $g\text{-}C_3N_4$, and CO_2 is reduced to CH_4 and CO on the CB of TiO_2. The efficient charge carrier transfer in the $g\text{-}C_3N_4/TiO_2$ heterojunction enhances the photocatalytic CO_2 reduction performance.

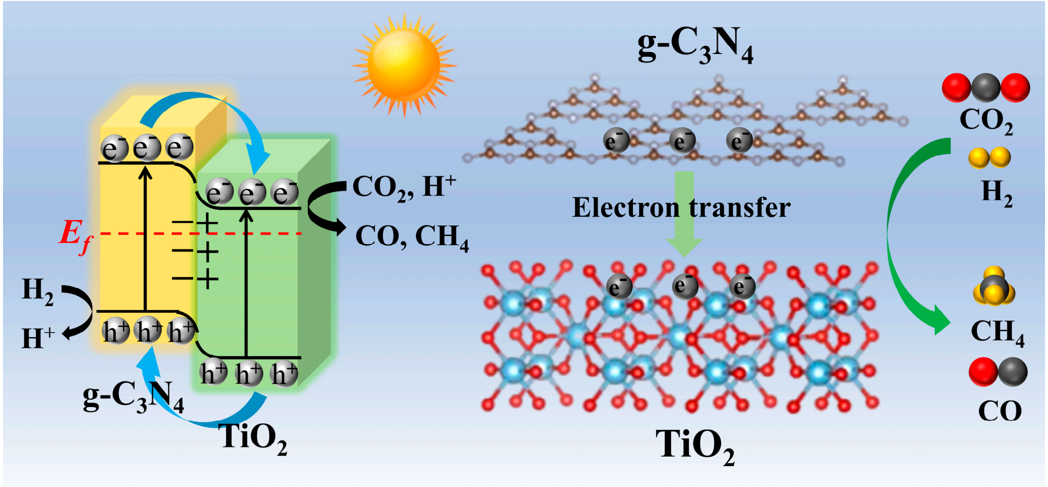

Figure 7. Schematic diagram of photocatalytic CO_2 reduction over $g\text{-}C_3N_4/TiO_2$.

3. Materials and Methods

3.1. Materials

Melamine ($C_3H_6N_6$) and titanium butoxide ($C_{16}H_{36}O_4Ti$) were obtained from Shanghai Aladdin Biochemical Technology Co., Ltd. (Shanghai, China). Absolute alcohol was purchased from Sinopharm Chemical Reagent Co., Ltd. (Shanghai, China). All chemicals were used without further purification.

3.2. Synthesis of g-C_3N_4/TiO_2

A total of 2 g of melamine was put into the crucible and then calcinated at 550 °C for 5 h with a ramp rate of 2.5 °C min^{-1} in a muffle furnace. After cooling to room temperature, bulk g-C_3N_4 was obtained. Bulk g-C_3N_4 was ground with a mortar to obtain g-C_3N_4 powder. Next, 0.5 g of g-C_3N_4 powder was dispersed into 100 mL of absolute alcohol under magnetic stirring for 2 h. Then, 5 mL of titanium butoxide was added into the above obtained suspension under magnetic stirring for 6 h. Finally, the mixture was calcinated at 550 °C for 5 h with a ramp rate of 2.5 °C min^{-1} in a muffle furnace to obtain g-C_3N_4/TiO_2. TiO_2 was prepared in the same way without the addition of g-C_3N_4 powder.

3.3. Characterization

The microstructures of g-C_3N_4, TiO_2 and g-C_3N_4/TiO_2 were observed by FSEM (Hitach S-4800, Tokyo, Japan) and TEM (Talos F200S, New York, NY, USA). The XRD patterns of g-C_3N_4, TiO_2, and g-C_3N_4/TiO_2 were obtained by an X-ray diffraction machine (Bruker D8 Advance, Billerica, MA, USA) using Cu Kα (λ = 0.15418 nm) radiation. The X-ray photoelectron spectroscopy (XPS; Omicron Sphera II, Taunusstein, Germany) data of g-C_3N_4, TiO_2, and g-C_3N_4/TiO_2 were obtained on a mono-chromated Al Kα X-ray source (hv = 1486.6 eV) at 15 kV/150 W to detect the chemical states of the elements in the samples. Nitrogen adsorption isotherms and the Brunauer–Emmett–Teller (BET) surface areas of g-C_3N_4, TiO_2, and g-C_3N_4/TiO_2 were obtained with a nitrogen adsorption apparatus (TriStar II 2020, Micromeritics, Norcross, GA, USA). The UV–vis diffuse reflectance spectra (UV–vis DRS) of g-C_3N_4, TiO_2, and g-C_3N_4/TiO_2 were acquired by a UV–VIS-NIR spectrometer (Lambda 750S; PerkinElmer, Freehold, NJ, USA) over a range of 200–800 nm. Transient photocurrent spectra (TPC), electrochemical impedance spectroscopy (EIS), and the Mott–Schottky (M-S) curve of g-C_3N_4, TiO_2, and g-C_3N_4/TiO_2 were measured with an electrochemical workstation (CS2350H; CorrTest, Wuhan, China) in 0.5 M Na_2SO_4 solution at room temperature by using a 300 W xenon lamp (PLS-SXE300; PerfectLight, Beijing, China). A Pt plate and Ag/AgCl were employed as the counter electrode and the reference electrode, respectively. In situ time-resolved DRIFT spectra of g-C_3N_4/TiO_2 were obtained by a Fourier transform infrared spectrometer (VERTEX V80; Bruker, Hong Kong, China). The work functions of g-C_3N_4 and TiO_2 were calculated by density functional theory (DFT) in Materials Studio.

3.4. Photocatalytic CO_2 Reduction

A total of 100 mg of catalyst was placed into a 200 mL stainless steel reactor with an optical quartz window at the top. The reactor was firstly vacuumed; then, CO_2 and H_2 were introduced into the stainless steel reactor in a volume ratio of 1:4 for half an hour to blow out the air in the reactor. A 300 W xenon lamp (PLS-SXE300; Beijing PerfectLight, Beijing, China) with a filter (AM 1.5 G; Ceaulight Technology Co., Ltd., Beijing, China) was employed to simulate solar illumination at about 100 mW·cm^{-2}. The reactor was irradiated by a xenon lamp for the desired time. During the photocatalytic reaction process, the gaseous mixture was periodically sampled from the stainless steel reactor every 0.5 h and analyzed by gas chromatography.

4. Conclusions

In summary, the g-C_3N_4/TiO_2 heterojunction was successfully prepared by growing TiO_2 on g-C_3N_4 for enhanced photocatalytic CO_2 reduction. Compared with g-C_3N_4 and

TiO_2, the photocatalytic CO_2 reduction performance of g-C_3N_4/TiO_2 was significantly enhanced due to the efficient charge carrier transfer in the heterojunction. The electron transfer mechanism in the g-C_3N_4/TiO_2 heterojunction was verified by in situ irradiated XPS. The photogenerated electrons migrate from g-C_3N_4 to TiO_2, while holes transfer from TiO_2 to g-C_3N_4. The photogenerated electrons of the reduction photocatalyst (RP) with strong reduction ability in TiO_2 and the photogenerated holes of the oxidation photocatalyst (OP) with strong oxidation ability in g-C_3N_4 are preserved for photocatalytic CO_2 reduction. The pathway of the photocatalytic reduction of CO_2 to CH_4 and CO on g-C_3N_4/TiO_2 was revealed by in situ DRIFTS. The pathway of the photocatalytic reduction of CO_2 to CH_4 and CO over g-C_3N_4/TiO_2 is briefly expressed as $CO_2 \rightarrow COO^- \rightarrow HCHO^- \rightarrow CH_3O^- \rightarrow CH_4$ and $CO_2 \rightarrow COO^- \rightarrow CO$. Therefore, this work reveals the electron transfer mechanism in polymer/metallic oxide heterojunctions and provides a feasible approach to design polymer/metallic oxide heterojunctions with efficient electron transfer for enhanced photocatalytic CO_2 reduction.

Supplementary Materials: The following supporting information can be downloaded at: https://www.mdpi.com/article/10.3390/catal14060335/s1, Figure S1. Pore size distribution curves of g-C_3N_4, TiO_2, and g-C_3N_4/TiO_2, Figure S2: FESEM images of g-C_3N_4, Figure S3: FESEM images of TiO_2, Figure S4: XPS survey spectra of g-C_3N_4, TiO_2, and g-C_3N_4/TiO_2, Figure S5. Time-resolved PL spectra of g-C_3N_4, TiO_2, and g-C_3N_4/TiO_2, Figure S6. SEM images after the stability tests of g-C_3N_4/TiO_2, Figure S7. XRD patterns before and after the stability tests of g-C_3N_4/TiO_2, Table S1: Brunauer–Emmett–Teller surface areas (S_{BET}) of samples, Table S2. Performance comparison of TiO_2-based and g-C_3N_4-based photocatalytic materials for CO_2 reduction, Table S3. Different mixing rations of g-C_3N_4 and TiO_2 photocatalysts for CO_2 reduction. Refs. [45,50–53] are cited in Supplementary Materials.

Author Contributions: Conceptualization, P.J. and K.W.; methodology, W.L.; validation, P.J., K.W. and W.L.; formal analysis, P.J.; investigation, Y.Y.; resources, K.W.; data curation, W.L.; writing—original draft preparation, P.J.; writing—review and editing, Y.Y.; visualization, Y.Y.; supervision, Y.Y.; project administration, P.J. All authors have read and agreed to the published version of the manuscript.

Funding: This research received no external funding.

Data Availability Statement: Data will be made available upon request.

Conflicts of Interest: The authors declare no conflicts of interest.

References

1. Barral, A.; Gomez, B.; Fourel, F.; Daviero-Gomez, V.; Lécuyer, C. CO_2 and temperature decoupling at the million-year scale during the Cretaceous Greenhouse. *Sci. Rep.* **2017**, *7*, 8310. [CrossRef]
2. Nordt, L.; Breecker, D.; White, J. Jurassic greenhouse ice-sheet fluctuations sensitive to atmospheric CO_2 dynamics. *Nat. Geosci.* **2022**, *15*, 54–59. [CrossRef]
3. Ortega, T.; Jiménez-López, D.; Sierra, A.; Ponce, R.; Forja, J. Greenhouse gas assemblages (CO_2, CH_4 and N_2O) in the continental shelf of the Gulf of Cadiz (SW Iberian Peninsula). *Sci. Total Environ.* **2023**, *898*, 165474. [CrossRef] [PubMed]
4. Chen, B.; Tan, E.; Zou, W.; Han, L.-L.; Tian, L.; Kao, S.-J. The external/internal sources and sinks of greenhouse gases (CO_2, CH_4, N_2O) in the Pearl River Estuary and adjacent coastal waters in summer. *Water Res.* **2024**, *249*, 120913. [CrossRef] [PubMed]
5. Fang, S.; Rahaman, M.; Bharti, J.; Reisner, E.; Robert, M.; Ozin, G.A.; Hu, Y.H. Photocatalytic CO_2 reduction. *Nat. Rev. Methods Primers* **2023**, *3*, 61. [CrossRef]
6. Albero, J.; Peng, Y.; García, H. Photocatalytic CO_2 Reduction to C^{2+} Products. *ACS Catal.* **2020**, *10*, 5734–5749. [CrossRef]
7. Qu, T.; Wei, S.; Xiong, Z.; Zhang, J.; Zhao, Y. Progress and prospect of CO_2 photocatalytic reduction to methanol. *Fuel. Process. Technol.* **2023**, *251*, 107933. [CrossRef]
8. Low, J.; Zhang, C.; Karadas, F.; Xiong, Y. Photocatalytic CO_2 conversion: Beyond the earth. *Chin. J. Catal.* **2023**, *50*, 1–5. [CrossRef]
9. Zhao, J.; Xiong, Z.; Zhao, Y.; Chen, X.; Zhang, J. Two-dimensional heterostructures for photocatalytic CO_2 reduction. *Environ. Res.* **2023**, *216*, 114699. [CrossRef]
10. Zhang, J.; Shi, J.; Tao, S.; Wu, L.; Lu, J. Cu_2O/Ti_3C_2MXene heterojunction photocatalysts for improved CO_2 photocatalytic reduction performance. *Appl. Surf. Sci.* **2021**, *542*, 148685. [CrossRef]
11. Liu, J.; Liu, Y.; Li, L.; Ye, X.; Zheng, X.; Pan, L.; Ren, W.; Meng, S.; Zhang, S.; Chen, S. Tailoring defects in In_2S_3/Zn0.3$Cd_{0.7}$S heterojunctions for efficient photocatalytic CO_2 conversion. *Appl. Surf. Sci.* **2023**, *631*, 157524. [CrossRef]

12. Guo, R.-t.; Guo, S.-h.; Yu, L.-q.; Pan, W.-g. Recent Progress and Perspectives of S-Scheme Heterojunction Photocatalysts for Photocatalytic CO_2 Reduction. *Energy. Fuels* **2024**, *38*, 869–894. [CrossRef]
13. Wang, L.; Dong, Y.; Zhang, J.; Tao, F.; Xu, J. Construction of NiO/g-C_3N_4 p-n heterojunctions for enhanced photocatalytic CO_2 reduction. *J. Solid. State. Chem.* **2022**, *308*, 122878. [CrossRef]
14. Ye, L.; Wu, D.; Chu, K.H.; Wang, B.; Xie, H.; Yip, H.Y.; Wong, P.K. Phosphorylation of g-C_3N_4 for enhanced photocatalytic CO_2 reduction. *Chem. Eng. J.* **2016**, *304*, 376–383. [CrossRef]
15. Sun, Z.; Wang, H.; Wu, Z.; Wang, L. g-C_3N_4 based composite photocatalysts for photocatalytic CO_2 reduction. *Catal. Today.* **2018**, *300*, 160–172. [CrossRef]
16. Ghosh, U.; Majumdar, A.; Pal, A. Photocatalytic CO_2 reduction over g-C_3N_4 based heterostructures: Recent progress and prospects. *J. Environ. Chem. Eng.* **2021**, *9*, 104631. [CrossRef]
17. Wei, L.; Yu, C.; Zhang, Q.; Liu, H.; Wang, Y. TiO_2-based heterojunction photocatalysts for photocatalytic reduction of CO_2 into solar fuels. *J. Mater. Chem. A* **2018**, *6*, 22411–22436. [CrossRef]
18. Xiong, Z.; Lei, Z.; Li, Y.; Dong, L.; Zhao, Y.; Zhang, J. A review on modification of facet-engineered TiO_2 for photocatalytic CO_2 reduction. *J. Photoch. Photobio. C* **2018**, *36*, 24–47. [CrossRef]
19. Abdullah, H.; Khan, M.M.R.; Ong, H.R.; Yaakob, Z. Modified TiO_2 photocatalyst for CO_2 photocatalytic reduction: An overview. *J. CO2 Util.* **2017**, *22*, 15–32. [CrossRef]
20. Feng, Y.; Wang, C.; Cui, P.; Li, C.; Zhang, B.; Gan, L.; Zhang, S.; Zhang, X.; Zhou, X.; Sun, Z.; et al. Ultrahigh Photocatalytic CO_2 Reduction Efficiency and Selectivity Manipulation by Single-Tungsten-Atom Oxide at the Atomic Step of TiO_2. *Adv. Mater.* **2022**, *34*, 2109074. [CrossRef]
21. Adekoya, D.O.; Tahir, M.; Amin, N.A.S. g-C_3N_4/(Cu/TiO_2) nanocomposite for enhanced photoreduction of CO_2 to CH_3OH and HCOOH under UV/visible light. *J. CO2 Util.* **2017**, *18*, 261–274. [CrossRef]
22. Banitalebi Dehkordi, A.; Ziarati, A.; Ghasemi, J.B.; Badiei, A. Preparation of hierarchical g-C_3N_4@TiO_2 hollow spheres for enhanced visible-light induced catalytic CO_2 reduction. *Solar. Energy* **2020**, *205*, 465–473. [CrossRef]
23. Hammoud, L.; Marchal, C.; Colbeau-Justin, C.; Toufaily, J.; Hamieh, T.; Caps, V.; Keller, V. Tuning CH4 Productivity from Visible Light-Driven Gas-Phase CO_2 Photocatalytic Reduction on Doped g-C_3N_4/TiO_2 Heterojunctions. *Energy Technol.* **2023**, *11*, 2201363. [CrossRef]
24. Kumar, D.P.; Rangappa, A.P.; Shim, H.S.; Do, K.H.; Hong, Y.; Gopannagari, M.; Reddy, K.A.J.; Bhavani, P.; Reddy, D.A.; Song, J.K.; et al. Nanocavity-assisted single-crystalline Ti^{3+} self-doped blue TiO_2(B) as efficient cocatalyst for high selective CO_2 photoreduction of g-C_3N_4. *Mater. Today Chem.* **2022**, *24*, 100827. [CrossRef]
25. Liu, C.; Raziq, F.; Li, Z.; Qu, Y.; Zada, A.; Jing, L. Synthesis of TiO_2/g-C_3N_4 nanocomposites with phosphate–oxygen functional bridges for improved photocatalytic activity. *Chin. J. Catal.* **2017**, *38*, 1072–1078. [CrossRef]
26. Mehregan, S.; Hayati, F.; Mehregan, M.; Isari, A.A.; Jonidi Jafari, A.; Giannakis, S.; Kakavandi, B. Exploring the visible light–assisted conversion of CO_2 into methane and methanol, using direct Z-scheme TiO_2@g-C_3N_4 nanosheets: Synthesis and photocatalytic performance. *Environ. Sci. Pollut. Res.* **2022**, *29*, 74951–74966. [CrossRef] [PubMed]
27. Park, J.; Liu, H.; Piao, G.; Kang, U.; Jeong, H.W.; Janáky, C.; Park, H. Synergistic conversion of CO_2 into C_1 and C_2 gases using hybrid in-doped TiO_2 and g-C_3N_4 photocatalysts. *Chem. Eng. J.* **2022**, *437*, 135388. [CrossRef]
28. Shi, H.; Du, J.; Hou, J.; Ni, W.; Song, C.; Li, K.; Gurzadyan, G.G.; Guo, X. Solar-driven CO_2 conversion over Co^{2+} doped 0D/2D TiO_2/g-C_3N_4 heterostructure: Insights into the role of Co^{2+} and cocatalyst. *J. CO2 Util.* **2020**, *38*, 16–23. [CrossRef]
29. Thanh Truc, N.T.; Giang Bach, L.; Thi Hanh, N.; Pham, T.-D.; Thi Phuong Le Chi, N.; Tran, D.T.; Nguyen, M.V.; Nguyen, V.N. The superior photocatalytic activity of Nb doped TiO_2/g-C_3N_4 direct Z-scheme system for efficient conversion of CO_2 into valuable fuels. *J. Colloid. Interf. Sci.* **2019**, *540*, 1–8. [CrossRef]
30. Tong, Z.; Hai, Y.; Wang, B.; Lv, F.; Zhong, Z.; Xiong, R. Activated g-C_3N_4 Photocatalyst with Defect Engineering for Efficient Reduction of CO_2 in Water. *J. Phys. Chem. C* **2023**, *127*, 11067–11075. [CrossRef]
31. Wang, C.; Zhao, Y.; Xu, H.; Li, Y.; Wei, Y.; Liu, J.; Zhao, Z. Efficient Z-scheme photocatalysts of ultrathin g-C_3N_4-wrapped Au/TiO_2-nanocrystals for enhanced visible-light-driven conversion of CO_2 with H_2O. *Appl. Catal. B-Environ.* **2020**, *263*, 118314. [CrossRef]
32. Yu, Y.; Hoshyar, A.N.; Samali, B.; Zhang, G.; Rashidi, M.; Mohammadi, M. Corrosion and coating defect assessment of coal handling and preparation plants (CHPP) using an ensemble of deep convolutional neural networks and decision-level data fusion. *Neural. Comput. Appl.* **2023**, *35*, 18697–18718. [CrossRef]
33. Yu, Y.; Zhang, C.; Xie, X.; Yousefi, A.M.; Zhang, G.; Li, J.; Samali, B. Compressive strength evaluation of cement-based materials in sulphate environment using optimized deep learning technology. *Dev. Built Environ.* **2023**, *16*, 100298. [CrossRef]
34. Zhang, H.; Bian, H.; Wang, F.; Zhu, L.; Zhang, S.; Xia, D. Enhanced photocatalytic reduction of CO_2 over pg-C_3N_4-supported TiO_2 nanoparticles with Ag modification. *Colloid. Surf. A* **2023**, *674*, 131989. [CrossRef]
35. Zhou, S.; Liu, Y.; Li, J.; Wang, Y.; Jiang, G.; Zhao, Z.; Wang, D.; Duan, A.; Liu, J.; Wei, Y. Facile in situ synthesis of graphitic carbon nitride (g-C_3N_4)-N-TiO_2 heterojunction as an efficient photocatalyst for the selective photoreduction of CO_2 to CO. *Appl. Catal. B-Environ.* **2014**, *158–159*, 20–29. [CrossRef]
36. Dong, W.-W.; Jia, J.; Wang, Y.; An, J.-R.; Yang, O.-Y.; Gao, X.-J.; Liu, Y.-L.; Zhao, J.; Li, D.-S. Visible-light-driven solvent-free photocatalytic CO_2 reduction to CO by Co-MOF/Cu_2O heterojunction with superior selectivity. *Chem. Eng. J.* **2022**, *438*, 135622. [CrossRef]

37. Huang, Y.; Li, D.; Fang, Z.; Chen, R.; Luo, B.; Shi, W. Controlling carbon self-doping site of g-C_3N_4 for highly enhanced visible-light-driven hydrogen evolution. *Appl. Catal. B-Environ.* **2019**, *254*, 128–134. [CrossRef]
38. Ma, X.; Liu, Y.; Wang, Y.; Jin, Z. Co_3O_4/CeO_2 p-n heterojunction construction and application for efficient photocatalytic hydrogen evolution. *Int. J. Hydrogen Energy* **2021**, *46*, 33809–33822. [CrossRef]
39. Shi, W.; Hao, C.; Fu, Y.; Guo, F.; Tang, Y.; Yan, X. Enhancement of synergistic effect photocatalytic/persulfate activation for degradation of antibiotics by the combination of photo-induced electrons and carbon dots. *Chem. Eng. J.* **2022**, *433*, 133741. [CrossRef]
40. He, F.; Zhu, B.; Cheng, B.; Yu, J.; Ho, W.; Macyk, W. 2D/2D/0D TiO_2/C_3N_4/Ti_3C_2 MXene composite S-scheme photocatalyst with enhanced CO_2 reduction activity. *Appl. Catal. B-Environ.* **2020**, *272*, 119006. [CrossRef]
41. He, T.; Wang, L.; Fabregat-Santiago, F.; Liu, G.; Li, Y.; Wang, C.; Guan, R. Electron trapping induced electrostatic adsorption of cations: A general factor leading to photoactivity decay of nanostructured TiO_2. *J. Mater. Chem. A.* **2017**, *5*, 6455–6464. [CrossRef]
42. He, Z.; Han, Y.; Liu, S.; Cui, W.; Qiao, Y.; He, T.; Wang, Q. Toward the Intrinsic Superiority of Aligned One-Dimensional TiO_2 Nanostructures: The Role of Defect States in Electron Transport Process. *ChemElectroChem* **2020**, *7*, 4390–4397. [CrossRef]
43. Wang, L.; Tan, H.; Zhang, L.; Cheng, B.; Yu, J. In-situ growth of few-layer graphene on ZnO with intimate interfacial contact for enhanced photocatalytic CO_2 reduction activity. *Chem. Eng. J.* **2021**, *411*, 128501. [CrossRef]
44. Low, J.; Dai, B.; Tong, T.; Jiang, C.; Yu, J. In Situ Irradiated X-Ray Photoelectron Spectroscopy Investigation on a Direct Z-Scheme TiO_2/CdS Composite Film Photocatalyst. *Adv. Mater.* **2019**, *31*, e1802981. [CrossRef]
45. Wang, L.; Cheng, B.; Zhang, L.; Yu, J. In situ Irradiated XPS Investigation on S-Scheme TiO_2 @$ZnIn_2S_4$ Photocatalyst for Efficient Photocatalytic CO_2 Reduction. *Small* **2021**, *17*, e2103447. [CrossRef]
46. Zhang, P.; Li, Y.; Zhang, Y.; Hou, R.; Zhang, X.; Xue, C.; Wang, S.; Zhu, B.; Li, N.; Shao, G. Photogenerated Electron Transfer Process in Heterojunctions: In Situ Irradiation XPS. *Small Methods* **2020**, *4*, 2000214. [CrossRef]
47. Bie, C.; Zhu, B.; Xu, F.; Zhang, L.; Yu, J. In Situ Grown Monolayer N-Doped Graphene on CdS Hollow Spheres with Seamless Contact for Photocatalytic CO_2 Reduction. *Adv. Mater.* **2019**, *31*, e1902868. [CrossRef]
48. Deng, Y.; Wan, C.; Li, C.; Wang, Y.; Mu, X.; Liu, W.; Huang, Y.; Wong, P.K.; Ye, L. Synergy Effect between Facet and Zero-Valent Copper for Selectivity Photocatalytic Methane Formation from CO_2. *ACS Catal.* **2022**, *12*, 4526–4533. [CrossRef]
49. Yin, G.; Huang, X.; Chen, T.; Zhao, W.; Bi, Q.; Xu, J.; Han, Y.; Huang, F. Hydrogenated Blue Titania for Efficient Solar to Chemical Conversions: Preparation, Characterization, and Reaction Mechanism of CO_2 Reduction. *ACS Catal.* **2018**, *8*, 1009–1017. [CrossRef]
50. Xu, F.; Zhu, B.; Cheng, B.; Yu, J.; Xu, J. 1D/2D TiO_2/MoS_2 Hybrid Nanostructures for Enhanced Photocatalytic CO_2 Reduction. *Adv. Optical. Mater.* **2018**, *26*, 1800911. [CrossRef]
51. Bian, J.; Qu, Y.; Zhang, X.; Sun, N.; Tang, D.; Jing, L. Dimension-Matched Plasmonic Au/TiO_2/$BiVO_4$ Nanocomposites as Efficient Wide-Visible-Light Photocatalysts to Convert CO_2 and Mechanistic Insights. *J. Mater. Chem. A* **2018**, *6*, 11838–11845. [CrossRef]
52. Jia, Y.; Tong, X.; Zhang, J.; Zhang, R.; Yang, Y.; Zhang, L.; Ji, X. A facile synthesis of coral tubular g-C_3N_4 for photocatalytic degradation RhB and CO_2 reduction. *J. Alloy. Compd.* **2023**, *965*, 171432. [CrossRef]
53. Xu, X.; Huang, Y.; Dai, K.; Wang, Z.; Zhang, J. Non-noble-metal CuSe promotes charge separation and photocatalytic CO_2 reduction on porous g-C_3N_4 nanosheets. *Sep. Purif. Technol.* **2023**, *317*, 123887. [CrossRef]